ACS APPLIED MATERIALS & INTERFACES

www.acsami.org Research Article

Printed Electronic Devices with Inks of TiS_3 Quasi-One-Dimensional van der Waals Material

Saba Baraghani, Jehad Abourahma, Zahra Barani, Amirmahdi Mohammadzadeh, Sriharsha Sudhindra, Alexey Lipatov, Alexander Sinitskii, Fariborz Kargar,* and Alexander A. Balandin*

Cite This: https://doi.org/10.1021/acsami.1c12948 Read Online

ACCESS | Metrics & More | Article Recommendations | Supporting Information

ABSTRACT: We report on the fabrication and characterization of electronic devices printed with inks of quasi-one-dimensional (1D) van der Waals materials. The quasi-1D van der Waals materials are characterized by 1D motifs in their crystal structure, which allow for their exfoliation into bundles of atomic chains. The ink was prepared by the liquid-phase exfoliation of crystals of TiS_3 into quasi-1D nanoribbons dispersed in a mixture of ethanol and ethylene glycol. The temperature-dependent electrical measurements indicate that the electron transport in the printed devices is dominated by the electron hopping mechanisms. The low-frequency electronic noise in the printed devices is of $1/f^{\gamma}$-type with $\gamma \sim 1$ near-room temperature (f is the frequency). The abrupt changes in the temperature dependence of the noise spectral density and γ parameter can be indicative of the phase transition in individual TiS_3 nanoribbons as well as modifications in the hopping transport regime. The obtained results attest to the potential of quasi-1D van der Waals materials for applications in printed electronics.

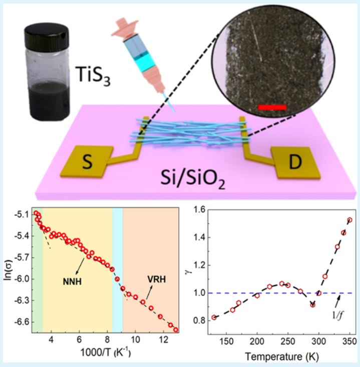

KEYWORDS: *quasi-1D materials, printed electronics, electron hopping conduction, low-frequency noise,* TiS_3

INTRODUCTION

Recent years have witnessed a boost in printed electronics research and development as the technique facilitates mass production of electronic devices with lower cost and processing requirements.[1,2] The approach also enables manufacturing of large-scale and flexible devices by expanding the choices of substrates from conventional silicon to flexible surfaces such as paper and textile.[3−5] Inks with proper thermophysical properties are the crucial component of the printing industry. Different functional materials have been developed and used as the ingredients for inks employed by various printing techniques. The printed electronic devices can find applications in various areas. Flexible radio frequency tags,[6] wearable electronics,[4] organic light-emitting diodes,[7] and organic solar cells[8] are just a few examples of such applications. Despite the recent advancements, however, the list of available materials as ingredients for inks is limited. Little is known about the nature of the charge transport and electronic noise characteristics in printed electronic devices.

Some of the previously demonstrated inks are based on metal nanoparticles, such as Ag,[9,10] Au,[11] and Cu,[12] carbon allotropes, such as graphene[13] and carbon nanotubes,[14] and nanowires, such as ZnO, dispersed in suitable solvents.[15] Most recently, attention has turned to the layered quasi-two-dimensional (2D) van der Waals (vdW) materials, such as transition metal dichalcogenides (TMDs), including MoS_2,[16,17] $MoSe_2$,[1] WS_2,[18] and Bi_2Te_3.[19] The class of quasi-2D vdW materials is promising for printing owing to relative ease of ink development. It is known that TMD materials have weak vdW bonding between structural units, allowing for their exfoliation into flexible quasi-2D layers. The inks of quasi-2D vdW materials can be prepared by liquid-phase exfoliation (LPE) process and dispersion of the exfoliated flakes in proper solvents. Additionally, TMDs exhibit tunable electronic and mechanical properties, which increase their value as ingredients for various functional inks.[20−25]

The class of layered vdW materials is not limited to quasi-2D materials only. Most recently, there has been a rapid emergence of interest in vdW materials with quasi-one-dimensional (1D) crystal structures.[26,27] These materials are quasi-1D in the sense that they have strong covalent bonds along the atomic chains and vdW bonds or substantially weaker covalent bonds in directions perpendicular to the chains.[28−30] Transition metal trichalcogenides (TMTs), with a chemical formula of MX_3, where M is a transition metal and X is a chalcogen, are a prominent group of quasi-1D vdW materials.[28−31] Examples of materials from this group include TiS_3,[32,33] $TaSe_3$,[28] ZrS_3,[32−35] NbS_3,[36] $ZrTe_3$,[37] and their solid solutions.[32] Unlike TMDs, which exfoliate into quasi-2D

Received: July 8, 2021
Accepted: September 12, 2021

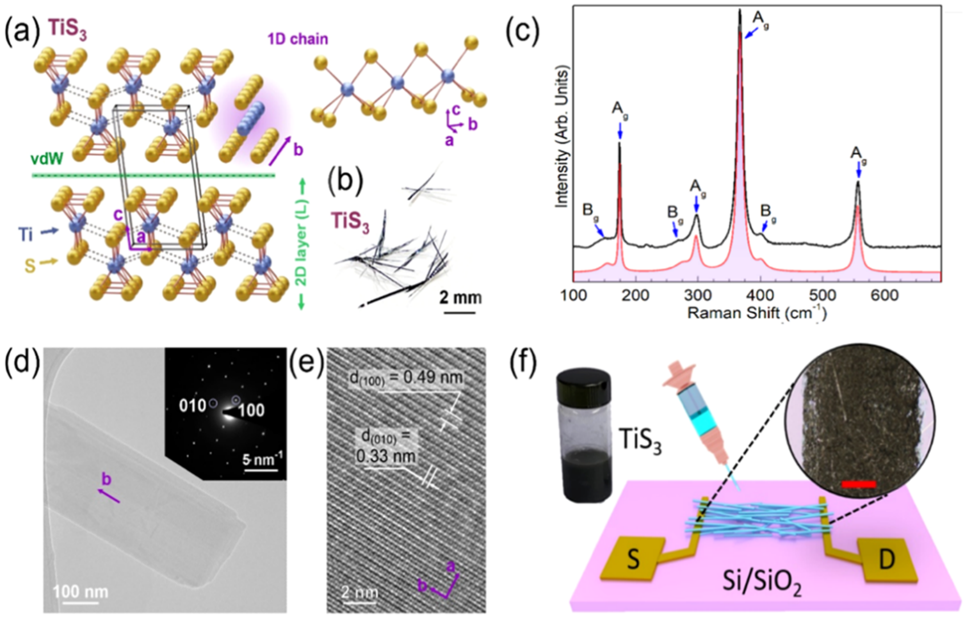

Figure 1. Crystal structure, sample preparation, and characterization. (a) Schematic of the monoclinic crystal structure of TiS_3 from two viewpoints. The blue and yellow spheres represent the Ti and S atoms, respectively. The parallelogram demonstrates the unit cell of TiS_3. The side view in the right panel exhibits the quasi-1D nature of the atomic chains. (b) Optical photograph of the TiS_3 crystals used in this study. (c) Raman spectrum of exfoliated TiS_3 (black curve) at room temperature. The red curve shows the cumulative fitting of the experimental data by individual Gaussian functions. (d) TEM image of a representative solution-exfoliated TiS_3 nanoribbon. A selected area electron diffraction (SAED) pattern recorded on this crystal is shown in the inset. (e) High-resolution TEM image of the same TiS_3 nanoribbon as in panel (d). (f) Schematic of the printing process of TiS_3 devices on top of gold contacts made with electron-beam lithography. The image in the dashed circle is the optical image of the actual TiS_3 device channel. Note the absence of the "coffee-ring" effect in the channel, confirming that the material is distributed evenly. The scale bar is 200 μm. The vial contains the liquid-phase exfoliated TiS_3 ink.

atomic planes, TMT crystals exfoliate into needle-like quasi-1D structures with high aspect ratios.[24,28,31,38] Motivated by the recent developments in the quasi-1D vdW material synthesis and exfoliation, we demonstrate the feasibility of the use of such materials in the inks for printed electronics. The high aspect ratio and flexibility of the exfoliated bundles of quasi-1D atomic chains offer specific advantages: possibly better connectivity of the individual flakes and smaller loading fractions required to achieve electrical conduction.[39,40]

The intrinsic properties of quasi-1D vdW metals and semiconductors can add to the unique ink functionalities. The exfoliated quasi-1D TMTs have demonstrated exceptional electrical properties. For example, the bundles of TiS_3, $TaSe_3$, and $ZrTe_3$ have shown exceptionally high breakdown current densities of ~1.7, ~10, and ~100 MA/cm^2, respectively.[41] For the present study, we selected TiS_3.[42−50] It is an n-type semiconductor with a band gap of ~1 eV at room temperature (RT).[43,45,49−51] The material undergoes a metal−insulator transition at temperature $T_M \sim 220$ K and exhibits metal-like properties at higher temperatures.[52] Bulk TiS_3 whiskers were shown to have the RT Hall mobility of about 30 cm^2 V^{-1} s^{-1}[46] and comparable exciton mobility of about 50 cm^2 V^{-1} s^{-1}.[53] Theoretically, it has been suggested that a single quasi-1D monolayer of TiS_3 can have a mobility of ~10 000 cm^2 V^{-1} s^{-1}, which is higher than that of quasi-2D MoS_2.[54] The experimentally observed mobilities in TiS_3 are considerably lower than the theoretical prediction, likely due to the polar-optical phonon scattering.[52,55] The few-layer TiS_3-based field-effect transistors (FETs) revealed mobilities of about 20−40 cm^2 V^{-1} s^{-1} and ON/OFF ratios of >10^3;[24] these experimental values are comparable to or higher than those in FETs based on few-layer MoS_2, which are ~10 to 20 cm^2 V^{-1} s^{-1}.[56,57] On the other hand, it has been reported that TiS_3 exhibits charge-density-wave phase transitions at low temperatures.[58] This feature, in addition to all other promising electrical characteristics, has made TiS_3 an interesting material to experiment with innovative inks for printed electronics. The use of quasi-1D TiS_3 can add new functionalities to the ink. A report on the LPE and drop-casting of TiS_3[59] suggested that this material might be suitable for ink printing if proper solvent is found and printing parameters are optimized.

The crystal structure of monoclinic TiS_3 with the $P2_1/m$ space group is presented in Figure 1a. Blue and yellow spheres represent the Ti and S atoms, respectively. The figure shows that TiS_3 has a highly anisotropic structure, in which quasi-1D chains of TiS_3 prisms are covalently bonded along the *b*-axis. These weakly interacting chains are assembled into vdW-stacked quasi-2D layers parallel to the *ab* plane of the crystal structure. A previous theoretical study has shown that the cleavage energies required for breaking weak interactions between the quasi-2D layers separated by the vdW gaps (Figure 1a) and between the quasi-1D chains within the layers are both comparable to the cleavage energy of graphene layers in graphite.[31] Because of this, a cleavage of a TiS_3 crystal may realistically proceed along several different planes between the quasi-1D chains (such as (001), (100), (101), etc.), resulting in the formation of high aspect ratio-exfoliated nanoribbons.[31]

EXPERIMENTAL SECTION

Materials. TiS_3 crystals were synthesized by the direct reaction between metallic titanium and a sulfur vapor in a vacuum-sealed quartz ampule at 550 °C, as described in our previous works.[24,53] Figure 1b shows an optical photograph of the as-grown TiS_3 crystals. Figure S1 presents the results of X-ray powder diffraction (XRD)

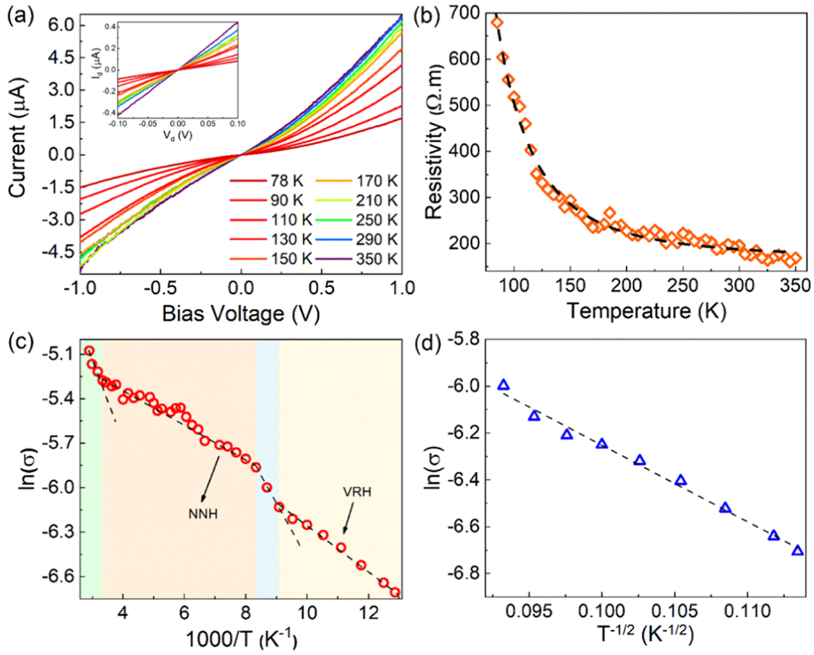

Figure 2. Electron transport mechanism in the devices printed with quasi-1D van der Waals ink. (a) Current−voltage characteristics of the TiS_3 printed device as a function of temperature. The inset shows the linear I−V dependence at small bias voltages. At higher voltages, the I−V curves become nonlinear. (b) Electrical resistivity of the printed TiS_3 channel as a function of temperature. The decrease in resistivity with temperature increase is consistent with the electron hopping transport mechanism. (c) Arrhenius plot of the electrical conductivity of the printed TiS_3 channel. The different shades of colors in the plot indicate changes in the conduction mechanism from nearest-neighbor hopping (NNH) to variable-range hopping (VRH). (d) Plot of ln(σ) versus $T^{-1/2}$ for the printed device channel at low temperatures. The experimental data agrees with the theoretical Efros−Shklovskii variable-range hoping model (dashed line).

measurements of the synthesized TiS_3 material. The pattern shows clear evidence of preferential orientation due to the stacking of the material. The XRD pattern presented in Figure S1, along with its Le Bail refinement, demonstrates the high purity of the material. Because of the highly anisotropic crystal structure (Figure 1a), the TiS_3 crystals are needle-shaped, with their long axes corresponding to the crystallographic b direction of the quasi-1D TiS_3 chains. The LPE process was performed on these TiS_3 crystals in ethanol, resulting in the cleavage of the bundles of the atomic chains, which appeared as needle-like nanoribbons. The details of the LPE process can be found in the Methods Section.

Characterization of Exfoliated TiS_3 Nanoribbons. The solution-exfoliated quasi-1D TiS_3 nanoribbons were characterized by atomic force microscopy (AFM). A droplet of TiS_3 dispersion in ethanol was placed on a Si/SiO_2 and dried in air. The resulting TiS_3 nanoribbons on a substrate were imaged using an atomic force microscope (Bruker Dimension Icon). The analysis of the AFM images was carried out using Gwyddion software.[60] A representative AFM image is shown in Figure S2a. The solution-exfoliated TiS_3 particles generally had ribbon-like shapes, which is representative of the quasi-1D structure of TiS_3. The thickness of these nanoribbons varied from several hundred nm down to several nm, as illustrated by the AFM height profile in Figure S2b. The material quality after the exfoliation processing steps has been confirmed with Raman spectroscopy (Renishaw inVia). The measurements were performed in the backscattering configuration under a visible red laser (λ = 633 nm). The laser spot size on the sample was ∼1 μm. The excitation power on the sample's surface was varied between 0.1 mW and 2 mW. After each measurement, the samples were carefully inspected using optical microscopy. No laser-induced changes in the samples were detected.

Figure 1c presents the Raman spectrum of exfoliated TiS_3 bundles at RT. The monoclinic structure of TiS_3 has C_{2h} point symmetry with irreducible representation of $\Gamma = 8A_g + 4B_g + 8B_u + 4A_u$. Four dominant Raman peaks identified at 174, 297, 367, and 556 cm^{-1} belong to A_g vibrational symmetries.[30,31,61] The peak at 174 cm^{-1} is associated with rigid chain vibrations.[61] The two peaks at 297 and 367 cm^{-1} are related to the internal out-of-plane vibrations involving each monolayer. The peak at 556 cm^{-1} is attributed to S−S diatomic motions.[61] The three low-intensity peaks at 163, 276, and 401 cm^{-1} that shoulder to the dominant Raman peaks belong to B_g vibrational symmetries.[62,63] The Raman spectra confirm the material quality after the exfoliation processing steps. To further confirm the high quality and crystallinity of the solution-exfoliated TiS_3 nanoribbons, we studied them by transmission electron microscopy (TEM) (FEI Tecnai Osiris). TEM image of a representative TiS_3 nanoribbon is shown in Figure 1d. A selected area electron diffraction (SAED) pattern recorded on this nanoribbon (see the inset in Figure 1d) confirms that it is highly crystalline. According to the indexing of the diffraction spots in this SAED pattern, the observed view corresponds to the ab plane of TiS_3. The long axis of the crystal represents the crystallographic b direction of the quasi-1D chains, which is in agreement with the most expected exfoliation scenario.[31] A high-resolution TEM image shown in Figure 1e, which was recorded for the same nanoribbon, confirms that this is the ab plane, because the observed interplanar distances perfectly match the a and b crystal structure parameters of TiS_3 (a = 0.4948 nm, b = 0.3379 nm, c = 0.8748 nm, and the cant angle β = 97.62°; see the crystallographic analysis in ref 24).

Ink Preparation and Device Printing. A schematic of the printing procedure and device is shown in Figure 1f. The electrodes were fabricated by e-beam lithography, followed by the liftoff of Ti/Au (20-nm/200-nm) deposited by e-beam evaporation. The TiS_3 channel was printed by a three-dimensional (3D) printer (Hyrel 30M) on top of the electrodes (see Figure S3). The thermophysical properties of the ink and proper selection of the injecting nozzle size play a crucial role in the ink droplet formation, even spreading of the ink on the substrate, and subsequent drying. The nonuniform deposition of the material in printing often happens as a result of the "coffee-ring" effect that should be avoided by adjusting the concentration of the ingredients in the ink and surface modification of the substrate.[64] The droplet formation behavior is characterized by

https://doi.org/10.1021/acsami.1c12948

a dimensionless Z-number (inverse of Ohnesorge number),[65,66] $Z = \sqrt{\zeta \rho a}/\mu$, where a is the printer's nozzle diameter [m], ζ, ρ, and μ are the surface tension [N m^{-1}], density [kg m^{-3}], and dynamic viscosity [Pa × s] of the ink, respectively. Generally, proper droplet formation and dispensing occur in the range of $1 \leq Z \leq 14$. Otherwise, satellite droplet formation ($Z > 14$) or elongated ligaments ($Z < 1$) may deteriorate the accuracy of the printing by deposition of the ink on undesired areas.[65,67−69] However, there are studies that report quality printings with $Z \geq 14$, especially for nanomaterial-based inks. For example, graphene-based inks with $Z \sim 24$ or polystyrene-nanoparticle-based inks with $Z \sim 21$ to ~91 have been successfully printed.[67,70−73] Therefore, the Z-number limits seem not to be strict for vdW materials, and inks with Z-number values close to the range guarantee proper printing quality.

To tune the Z-number for printing with quasi-1D vdW ink, we used a syringe with an inner diameter of a = 210 μm. The exfoliated TiS_3 bundles of atomic chains were mixed in ethanol with ethylene glycol (EG), using the mixing proportion of 1:1 (vol %). The dynamic viscosity, surface tension, and the mass density of the ink were measured to be $\zeta \sim 3.3$ [N m^{-1}], $\mu \sim 3.35 \times 10^{-3}$ [Pa × s], and $\rho \sim 949.6$ [kg m^{-3}], respectively. The details of the measurements can be found in the Methods section and the Supporting Information. The Z-number of the prepared ink was $Z \sim 24$. No satellite droplet formation or elongated ligaments were observed during the printing. Addition of EG helped to circumvent the "coffee-ring".[74] A faster evaporation rate of ethanol causes enrichment of the droplet contact line with EG, leading to a surface tension gradient in the droplet and uniform dispersion of the material while drying.[2,69] Optical images of two printed channels with and without the addition of EG are shown in Figure S4a,b. As seen, the addition of EG results in the elimination of the coffee-ring effect. To augment the flow through the ink droplet, the bed temperature of the printer was kept at 60 °C. The printed channel has the dimensions of 4 μm × 500 μm × 6 μm ($L \times W \times t$). The average thickness of the device was measured using an optical profilometer. A scanning electron microscopy (SEM) image of the channel as well as the surface profile of the channel are shown in Figure S5a,b.

RESULTS AND DISCUSSION

The electrical current−voltage (I−V) characteristics of the fabricated two-terminal devices were measured in the temperature range from 78 to 350 K. The I−V results are presented in Figure 2a. The weakly nonlinear I−V curves were attributed to the presence of the Schottky barrier at the printed channel−metal contact interface. Interestingly, it was previously shown that Au forms an Ohmic contact with TiS_3,[75] provided that there is a clean ultrahigh-vacuum-enabled interface between the two materials, resulting in strong Au−S interactions. The presence of Schottky barrier for these devices can be explained by the fabrication process, where the interfaces between the printed TiS_3 nanoribbons and the Ti/Au pads contain various surface adsorbates and residual solvent molecules. At low bias voltage, from −0.1 to 0.1 V, the I−V characteristics can be considered approximately linear (see the inset to Figure 2a). The resistivity of the printed TiS_3 channel was extracted using a standard two-probe technique (see Methods) from the linear I−V region as a function of temperature (see Figure 2b). At RT, the resistivity of the printed devices was ~195 Ω × m. The resistivity values reported in the literature span a wide range from 0.02 to 200 Ω × m for individual exfoliated bundles of atomic chains, *i.e.*, nanoribbons and crystals with defects.[52,58,59] Note that our resistivity results include the contact resistance. The solvent residues can also affect the overall resistance of the channel. Given the disordered nature of the printed device, the extracted values of resistivity are reasonable and consistent with the data reported for individual nanoribbons.[52]

As one can see in Figure 2b, the resistivity continuously decreases with increasing temperature. This is in contrast with the data on the electrical resistivity measurements of bulk and mechanically exfoliated few-layer TiS_3 devices reported over an extended temperature range of 4−400 K.[43,46,47,52] In the latter case, the resistivity decreased with increasing the temperature up to ~250 K, which is typical for semiconductor materials. At temperatures above 250 K, TiS_3 exhibits metallic properties, *i.e.*, the resistivity increases with the temperature rise.[52] In printed devices, however, one would expect to have a network of randomly arranged exfoliated TiS_3 atomic chain bundles with many bundle to bundle interfaces, defects, and impurities resulting from the LPE process and subsequent printing. In this case, the electron hopping transport is more likely to be the main mechanism of electron conduction. The electrical conductivity due to electron hopping has smaller values than the bulk band conduction, and it increases with increasing temperature. We now analyze the resistivity data in more detail.

Several models have been proposed to describe electron hopping in disordered material systems.[76] In the nearest-neighbor hopping (NNH) model, the system is considered to have randomly distributed isoenergetic sites with a concentration of N_0 and the electron localization length of α so that $N_0\ \alpha \ll 1$. The electrical conduction is carried out by the charge carriers jumping between the nearest sites. The temperature dependence of the electrical conductivity in NNH mechanism, σ_{NNH}, is described by the equation $\sigma_{NNH} = \sigma_{0NNH} \exp(-E_{NNH}/k_B T)$, where k_B is the Boltzmann constant, σ_{0NNH} and E_{NNH} are the NNH conductivity constant and the NNH activation energy, respectively. This equation is similar to the equation for the electrical conductivity in the thermally-activated band-conduction model, $\sigma = \sigma_0 \exp(-E_a/k_B T)$, where E_a is the thermal activation energy. The main difference in the formalisms is that $E_{NNH} < E_a$ so that generally NNH occurs at rather high temperatures, where the thermal activation energy is not sufficient to excite electrons to the conduction band but enough to excite them to the available spatially separated energy sites between the conduction and valence bands. At the low-temperature limit, electron hopping is dominated by the variable-range hopping (VRH) mechanism,[76−80] where the upward transition of electrons between energetically distinct but spatially nearby states is less likely than the transition to states with energetically close but spatially farther away states. Our experimental data at low temperature can be better described with the Efros−Shklovskii VRH model[76,77,80] in which the hopping distance between the trap sites is not constant, and carriers can hop between the levels closer to the Fermi level.[77] The temperature-dependent conductivity in this model is described by the equation $\sigma = \sigma_{0ES} \exp[-(T_{ES}/T)^{1/2}]$, where σ_{0ES} and T_{ES} are parameters that depend on the localization length and dielectric constant of the material.[80]

Figure 2c shows the Arrhenius plot of the resistivity data in the entire examined temperature range.[77,81] The plot is divided into four regions shaded in yellow, blue, orange, and green colors. The blue and green regions correspond to the temperature ranges, where the slope of the resistivity changes significantly. The change in the slope of the curve in the blue region is a signature of transitioning from VRH (yellow) to NNH (orange) conduction in disordered materials.[78,82−85] The activation energy calculated for the NNH conduction is ~12.4 meV. As expected, the extracted value is significantly

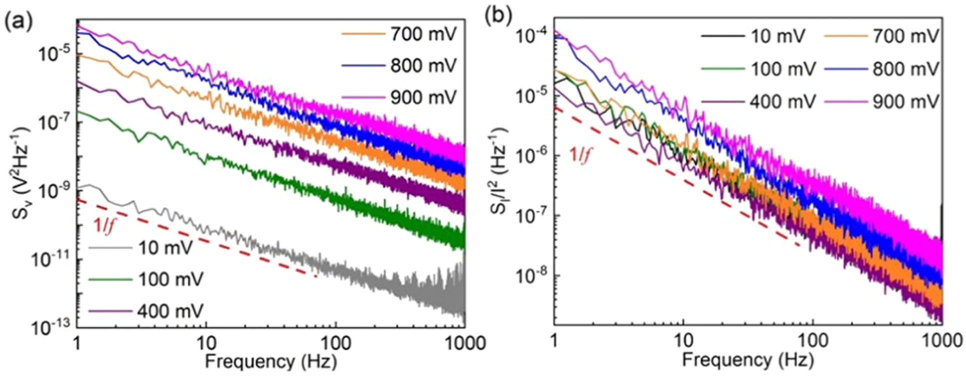

Figure 3. Room-temperature electronic noise spectroscopy of the printed devices. (a) Voltage-referred noise power spectral density and (b) normalized current noise power spectral density as a function of frequency at different applied bias voltages. The data in (a) and (b) follows 1/*f* noise dependency.

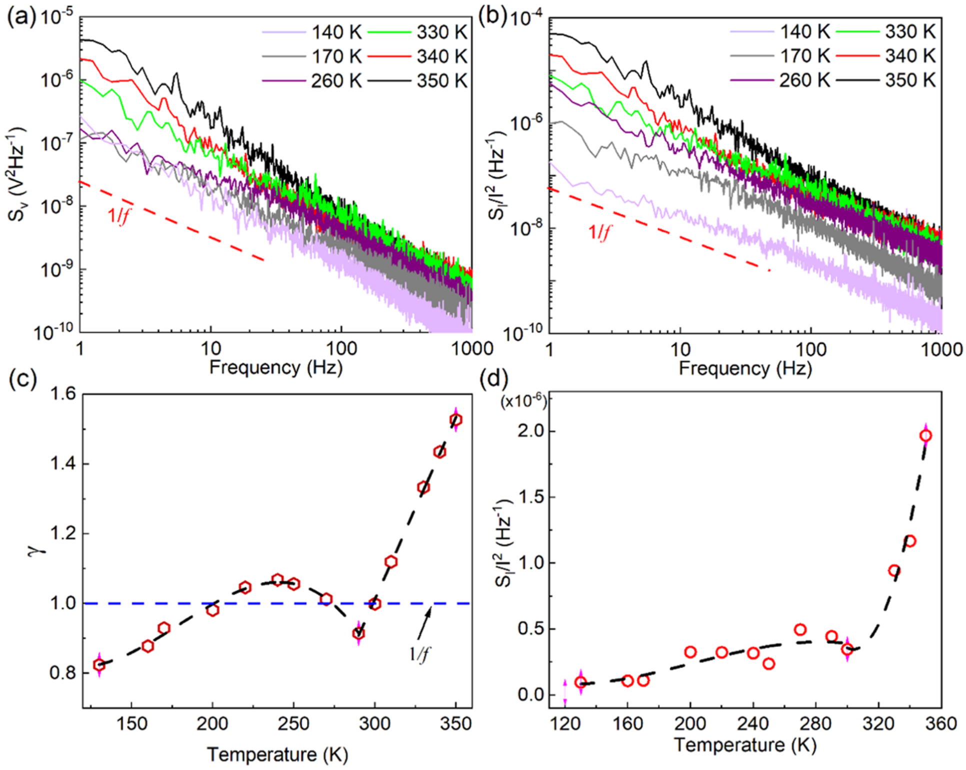

Figure 4. Temperature-dependent low-frequency electronic noise characteristics of the printed devices. (a) Low-frequency noise spectra of voltage fluctuations, S_V, as a function of frequency measured at different temperatures. (b) Normalized current noise spectral density as a function of frequency for various temperatures. (c) Extracted values of γ as a function of temperature. (d) Normalized noise spectral density versus temperature at the constant frequency of f = 10 kHz.

lower than the thermal activation energy reported for the bulk TiS_3 crystals, which is ~43 meV.[44,46,52] The data deviates from the NNH model at the high-temperature region again (see the green area in Figure 2c). The reason for such a deviation needs further investigation. Some previous studies have reported that bulk crystals of TiS_3 are likely to undergo the charge density wave (CDW) phase transitions at ~60 K and ~220 K.[52,58] The high-temperature phase transition in bulk form can happen in the temperature range between 200 K to 260 K, depending on the quality of the sample.[58] The reported phase transition temperatures are close to the transition regions, which we have marked in green and blue colors in Figure 2c. Figure 2d shows the resistivity data as a function of $T^{-1/2}$ in the temperature range from 78 to 115 K, where VRH conduction dominates. According to the Efros−Shklovskii VRH model, the plot of ln(σ) as a function of $T^{-1/2}$ must be linear. One can see an excellent agreement between our experimental data and the fitted linear regression in this temperature range.

We used low-frequency electronic noise spectroscopy to further elucidate the electron transport properties in our printed devices. The details of our experimental setup and measurement procedures have been reported elsewhere in the context of other material systems.[84,86] The analysis of the noise spectral density, its functional dependence on frequency, electric bias, and temperature can provide a wealth of information on the electron transport, particularly in material systems with high concentrations of defects and impurities, which act at the charge trapping sites. We have successfully used electronic noise spectroscopy for monitoring phase transitions in materials, which reveal strongly correlated phenomena.[84,87−90] Typically, at the frequencies $f < 100$ kHz, materials show the spectral noise density of $S(f) \sim 1/f^{\gamma}$ type, with $\gamma \sim 1$. In Figure 3a,b we present the voltage-referred noise power spectral density, S_v, and the normalized current noise power spectral density, S_I/I^2, for the device channel printed with the quasi-1D TiS_3 ink as a function of frequency. The noise spectra were measured for several bias voltages at RT. One can see that the noise generally follows the $1/f$ trend, and it increases with the increase in bias voltage as expected.[84,87,90] There are some traces of Lorentzian-type bulges at frequencies above $f = 100$ Hz. They can indicate the presence of certain defects or impurities with a particularly high concentration that act as the trapping centers for the charge carriers contributing to the current conduction. If such a defect with a characteristic time constant of the charge carrier trapping and de-trapping dominates the current fluctuations, its contribution to the noise spectrum appears as a Lorentzian bulge.[91]

Figure 4a,b shows the voltage noise spectral density, S_v, and the normalized current spectral density, S_I/I^2, as a function of temperature. All measurements were carried out with a small applied bias of ∼0.3 V to avoid Joule heating. The spectra in both plots follow the $1/f^{\gamma}$. However, γ is no longer close to 1, and it reveals a rather strong functional dependence on temperature. Figure 4c shows the extracted values of γ as a function of temperature in the range between 130 K to 350 K. The black dashed lines are eye guides only. The observed large deviation of γ from 1 can be related to the Lorentzian bulges (see Figure 4a,b), which are more pronounced at low and high temperature limits. The changes in the noise spectra can be associated with the reported metal−insulator transition at temperature $T_M \sim 250$ K[52] as well as the change in the electron hopping conductivity around $T \sim 320$ K (see the green region in Figure 2c). Figure 4d shows the normalized noise spectral density, S_I/I^2, as a function of temperature at the fixed frequency of 10 Hz. The noise level abruptly increases at the temperature of ∼320 K. This supports the hypothesis of changes in the electron hopping transport mechanism as seen in the resistivity data in Figure 2c and γ parameter dependence in Figure 4c.

CONCLUSIONS

In conclusion, we report on printing electronic devices with inks of quasi-1D vdW materials. The ink was prepared by the LPE of small crystals of TiS_3 semiconductor into quasi-1D nanoribbons dispersed in a mixture of ethanol and ethylene glycol. The temperature-dependent electrical measurements indicate that electron transport in the printed devices is dominated by the electron hopping mechanisms. The low-frequency electronic noise in the printed devices is of $1/f^{\gamma}$-type with $\gamma \sim 1$ near room temperature (f is the frequency). The abrupt changes in temperature dependence of the noise spectral density and γ parameter can be indicative of the phase transition in individual TiS_3 nanoribbons as well as modifications in the hopping transport regime. The obtained results attest to the potential of quasi-1D vdW materials for applications in printed electronics. The developed printing process can also facilitate the characterization of new quasi-1D van der Waals materials predicted by machine learning studies, which are being currently synthesized.

METHODS

Liquid-Phase Exfoliation of TiS_3 Crystals. Liquid-phase exfoliation was conducted by placing 100 mg of TiS_3 crystals in a round-bottom flask with 50 mL of dry ethanol. The round-bottom flask was sealed with a septum and then placed in the center of a 40 kHz ultrasonic bath sonicator. Nitrogen gas was bubbled through the dispersion during the first hour of sonication to remove any dissolved oxygen. The dispersion was sonicated for a total of 24 h, sealed under nitrogen gas. After exfoliation, the dispersion was transferred to a 20 mL dram vial. This transfer was conducted in a dry nitrogen-filled glovebox to prevent any oxygen or water contamination. The resulting dispersion of the liquid-phase exfoliated TiS_3 in ethanol had a concentration of 2 mg/mL.

TiS_3 Ink Preparation and Characterization. Briefly, 3 mL of 4 mg/mL exfoliated TiS_3 in ethanol was mixed with 3 mL of ethylene glycol (EG) to give 6 mL of 2 mg/mL TiS_3 in 1/1 vol % ethanol/ethylene glycol as the ink. TEM of the solution-exfoliated TiS_3 nanoribbons was performed using an FEI Tecnai Osiris scanning transmission electron microscope at the accelerating voltage of 200 kV. Ethylene glycol was added to the ink to increase the viscosity of the ink. This is to ensure proper dispensing and drying of the ink. The viscosity, surface tension, and density of the ink were measured to calculate the characteristic Z-number. To measure the viscosity, a CANNON SimpleVIS viscometer was used. Then, 0.5 μL of the ink was inserted into the device, and the measured kinematic viscosity was displayed on the device screen. Then, this value was divided by the density to calculate the dynamic viscosity. A CSC Scientific DuNouy interfacial tensiometer was used to calculate the surface tension of the ink. To measure the surface tension, the device ring was inserted in the ink. Then, the ring was raised slowly until the film between the ink and the ink broke. The surface tension value can be read from the device dial. With the addition of EG to the ink, the viscosity and surface tension of the ink were measured to be 3.346 mPa·s and 33.1 mN m^{-1}. The density of the ink was calculated using the rule of mixtures. The calculated density of the ink was 949.6 $kg \cdot m^{-3}$. With these values, the calculated Z-number of the ink is 24.28 for the nozzle with an inner diameter of 210 μm used in this work.

Printing Devices with Quasi-1D TiS_3 vdW Materials. The TiS_3 ink was used in a modified Hyrel 30M system 3D printer to print out the TiS_3 channel. To mimic the function of an inkjet printer, the printer head was swapped with a syringe holder. The holder controlled a blunt-end needle syringe with gauge 27 to dispense the ink on the substrate. The bed temperature of the printer was kept at 60 °C during the whole course of the printing process. Briefly, 20 layers of the material were printed on the substrate with the gold electrodes. The electrodes were fabricated by electron-beam lithography and liftoff of Ti/Au (20-nm/200-nm), deposited by electron-beam evaporation. The final TiS_3 channel had a length of 4 μm. The width and thickness of the channel were 500 μm and 6 μm, respectively.

Electrical Resistivity Measurements. We determined the resistance of the samples using a standard two-probe method. The current−voltage ($I-V$) characteristics were measured in the cryogenic probe station (Lake Shore TTPX) with a semiconductor analyzer (Agilent B1500). The resistance, R, was extracted from the linear part of the $I-V$ plots presented in Figure 1a. Assuming the isotropic properties in all directions, the resistivity was determined from the formula $\rho = RA/l$, where l and A were the channel length and the cross-sectional area, respectively. The thickness of the channel was measured with an optical profilometer, and the average cross section was calculated accordingly (see Supporting Information Section VI and Figure S5).

Noise spectroscopy. The low-frequency noise experiments were conducted in the two-terminal device configuration. The noise spectra were measured with a dynamic signal analyzer (Stanford Research 785). A battery biasing circuit was used to apply a bias voltage to the devices. This was done to minimize the noise at 60 Hz and the harmonics associated with it. The signal measured by the dynamic signal analyzer is the absolute voltage noise spectral density, S_v, of a parallel resistance network consisting of a load resistor (R_L) of 46 KΩ and the device under test with a resistance of R_D. The normalized current noise spectral density, S_I/I^2, was calculated by $S_I/I^2 = S_V \times [(R_L + R_D)/(R_L \times R_D)]^2/(I^2 \times G)$, where G is the amplification of the low-noise amplifier.

■ ASSOCIATED CONTENT

Supporting Information

The Supporting Information is available free of charge at https://pubs.acs.org/doi/10.1021/acsami.1c12948.

> A detailed description of the liquid-phase exfoliation and material characterization, printing, and device preparation, as well as electrical characterization of the device channel (PDF)

■ AUTHOR INFORMATION

Corresponding Authors

Fariborz Kargar − *Nano-Device Laboratory and Phonon Optimized Engineered Materials Center, Department of Electrical and Computer Engineering, University of California, Riverside, California 92521, United States; Department of Chemical and Environmental Engineering, University of California, Riverside, California 92521, United States;* orcid.org/0000-0003-2192-2023; Email: fkargar@ece.ucr.edu

Alexander A. Balandin − *Nano-Device Laboratory and Phonon Optimized Engineered Materials Center, Department of Electrical and Computer Engineering, University of California, Riverside, California 92521, United States; Department of Chemical and Environmental Engineering, University of California, Riverside, California 92521, United States*; Email: balandin@ece.ucr.edu

Authors

Saba Baraghani − *Nano-Device Laboratory and Phonon Optimized Engineered Materials Center, Department of Electrical and Computer Engineering, University of California, Riverside, California 92521, United States; Department of Chemical and Environmental Engineering, University of California, Riverside, California 92521, United States;* orcid.org/0000-0003-0256-0397

Jehad Abourahma − *Department of Chemistry, University of Nebraska, Lincoln, Nebraska 68588, United States*

Zahra Barani − *Nano-Device Laboratory and Phonon Optimized Engineered Materials Center, Department of Electrical and Computer Engineering, University of California, Riverside, California 92521, United States*

Amirmahdi Mohammadzadeh − *Nano-Device Laboratory and Phonon Optimized Engineered Materials Center, Department of Electrical and Computer Engineering, University of California, Riverside, California 92521, United States*

Sriharsha Sudhindra − *Nano-Device Laboratory and Phonon Optimized Engineered Materials Center, Department of Electrical and Computer Engineering, University of California, Riverside, California 92521, United States;* orcid.org/0000-0001-5299-3962

Alexey Lipatov − *Department of Chemistry, University of Nebraska, Lincoln, Nebraska 68588, United States;* orcid.org/0000-0001-5043-1616

Alexander Sinitskii − *Department of Chemistry, University of Nebraska, Lincoln, Nebraska 68588, United States; Nebraska Center for Materials and Nanoscience, University of Nebraska, Lincoln, Nebraska 68588, United States;* orcid.org/0000-0002-8688-3451

Complete contact information is available at: https://pubs.acs.org/10.1021/acsami.1c12948

Author Contributions

A.A.B. and F.K. conceived the idea, coordinated the project, contributed to experimental data analysis, and led the manuscript preparation; S.B. prepared the ink, printed the devices, conducted current−voltage and electronic noise measurements, and contributed to data analysis; J.A., A.L., and A.S. provided the TiS_3 crystals, characterized them by TEM, and contributed to the data analyses; A.M. contributed to electrode fabrication; Z.B. assisted with the material exfoliation and ink preparation and conducted Raman measurements; S.S. carried out thickness measurements by optical profilometer; All authors contributed to writing the manuscript.

Notes

The authors declare no competing financial interest.

■ ACKNOWLEDGMENTS

The work at UC Riverside was supported, in part, by the National Science Foundation (NSF) program Designing Materials to Revolutionize and Engineer our Future (DMREF) via a project DMR-1921958 entitled “Collaborative Research: Data Driven Discovery of Synthesis Pathways and Distinguishing Electronic Phenomena of 1D van der Waals Bonded Solids”. The work at UNL was supported by the NSF, through ECCS 1740136, as well as by the nCORE, which is a wholly-owned subsidiary of the Semiconductor Research Corporation (SRC), through the Center on Antiferromagnetic Magneto-electric Memory and Logic (AMML), task No. 2760.002.

■ REFERENCES

(1) Rowley-Neale, S. J.; Foster, C. W.; Smith, G. C.; Brownson, D. A. C.; Banks, C. E. Mass-Producible 2D-$MoSe_2$ Bulk Modified Screen-Printed Electrodes Provide Significant Electrocatalytic Performances towards the Hydrogen Evolution Reaction. *Sustainable Energy Fuels* **2017**, *1*, 74−83.

(2) Hu, G.; Yang, L.; Yang, Z.; Wang, Y.; Jin, X.; Dai, J.; Wu, Q.; Liu, S.; Zhu, X.; Wang, X.; Wu, T.-C.; Howe, R. C. T.; Albrow-Owen, T.; Ng, L. W. T.; Yang, Q.; Occhipinti, L. G.; Woodward, R. I.; Kelleher, E. J. R.; Sun, Z.; Huang, X.; Zhang, M.; Bain, C. D.; Hasan, T. A General Ink Formulation of 2D Crystals for Wafer-Scale Inkjet Printing. *Sci. Adv.* **2020**, *6*, No. eaba5029.

(3) Zschieschang, U.; Klauk, H. Organic Transistors on Paper: A Brief Review. *J. Mater. Chem. C* **2019**, *7*, 5522−5533.

(4) Bidoki, S.; McGorman, D.; Lewis, D.; Clark, M.; Horler, G.; Miles, R. E. Inkjet Printing of Conductive Patterns on Textile Fabrics. *AATCC Rev.* **2005**, *5*, 17−22.

(5) Carey, T.; Cacovich, S.; Divitini, G.; Ren, J.; Mansouri, A.; Kim, J. M.; Wang, C.; Ducati, C.; Sordan, R.; Torrisi, F. Fully Inkjet-Printed Two-Dimensional Material Field-Effect Heterojunctions for Wearable and Textile Electronics. *Nat. Commun.* **2017**, *8*, No. 1202.

(6) Redinger, D.; Molesa, S.; Yin, S.; Farschi, R.; Subramanian, V. An Ink-Jet-Deposited Passive Component Process for RFID. *IEEE Trans. Electron Devices* **2004**, *51*, 1978−1983.

(7) Park, S.-I.; Xiong, Y.; Kim, R.-H.; Elvikis, P.; Meitl, M.; Kim, D.-H.; Wu, J.; Yoon, J.; Yu, C.-J.; Liu, Z.; Huang, Y.; Hwang, K.; Ferreira, P.; Li, X.; Choquette, K.; Rogers, J. A. Printed Assemblies of Inorganic Light-Emitting Diodes for Deformable and Semitransparent Displays. *Science* **2009**, *325*, 977−981.

(8) Ganesan, S.; Mehta, S.; Gupta, D. Fully Printed Organic Solar Cells − a Review of Techniques, Challenges and Their Solutions. *Opto-Electron. Rev.* **2019**, *27*, 298−320.

(9) Jeong, S.; Song, H. C.; Lee, W. W.; Choi, Y.; Lee, S. S.; Ryu, B.-H. Combined Role of Well-Dispersed Aqueous Ag Ink and the Molecular Adhesive Layer in Inkjet Printing the Narrow and Highly Conductive Ag Features on a Glass Substrate. *J. Phys. Chem. C* **2010**, *114*, 22277−22283.

(10) Kosmala, A.; Wright, R.; Zhang, Q.; Kirby, P. Synthesis of Silver Nano Particles and Fabrication of Aqueous Ag Inks for Inkjet Printing. *Mater. Chem. Phys.* **2011**, *129*, 1075−1080.

(11) Määttänen, A.; Ihalainen, P.; Pulkkinen, P.; Wang, S.; Tenhu, H.; Peltonen, J. Inkjet-Printed Gold Electrodes on Paper: Characterization and Functionalization. *ACS Appl. Mater. Interfaces* **2012**, *4*, 955−964.

(12) Jeong, S.; Lee, S. H.; Jo, Y.; Lee, S. S.; Seo, Y.-H.; Ahn, B. W.; Kim, G.; Jang, G.-E.; Park, J.-U.; Ryu, B.-H.; Choi, Y. Air-Stable, Surface-Oxide Free Cu Nanoparticles for Highly Conductive Cu Ink and Their Application to Printed Graphene Transistors. *J. Mater. Chem. C* **2013**, *1*, 2704.

(13) Capasso, A.; Del Rio Castillo, A. E.; Sun, H.; Ansaldo, A.; Pellegrini, V.; Bonaccorso, F. Ink-Jet Printing of Graphene for Flexible Electronics: An Environmentally-Friendly Approach. *Solid State Commun.* **2015**, *224*, 53−63.

(14) Tortorich, R. P.; Choi, J.-W. Inkjet Printing of Carbon Nanotubes. *Nanomaterials* **2013**, *3*, 453−468.

(15) Wu, W. Inorganic Nanomaterials for Printed Electronics: A Review. *Nanoscale* **2017**, *9*, 7342−7372.

(16) Li, J.; Naiini, M. M.; Vaziri, S.; Lemme, M. C.; Östling, M. Inkjet Printing of MoS_2. *Adv. Funct. Mater.* **2014**, *24*, 6524−6531.

(17) Cho, B.; Yoon, J.; Lim, S. K.; Kim, A. R.; Kim, D.-H.; Park, S.-G.; Kwon, J.-D.; Lee, Y.-J.; Lee, K.-H.; Lee, B. H.; Ko, H. C.; Hahm, M. G. Chemical Sensing of 2D Graphene/MoS_2 Heterostructure Device. *ACS Appl. Mater. Interfaces* **2015**, *7*, 16775−16780.

(18) Kelly, A. G.; Hallam, T.; Backes, C.; Harvey, A.; Esmaeily, A. S.; Godwin, I.; Coelho, J.; Nicolosi, V.; Lauth, J.; Kulkarni, A.; Kinge, S.; Siebbeles, L. D. A.; Duesberg, G. S.; Coleman, J. N. All-Printed Thin-Film Transistors from Networks of Liquid-Exfoliated Nanosheets. *Science* **2017**, *356*, 69−73.

(19) Madan, D.; Wang, Z.; Chen, A.; Juang, R.; Keist, J.; Wright, P. K.; Evans, J. W. Enhanced Performance of Dispenser Printed MA N-Type Bi_2Te_3 Composite Thermoelectric Generators. *ACS Appl. Mater. Interfaces* **2012**, *4*, 6117−6124.

(20) Akinwande, D.; Petrone, N.; Hone, J. Two-Dimensional Flexible Nanoelectronics. *Nat. Commun.* **2014**, *5*, No. 5678.

(21) Franklin, A. D. Nanomaterials in Transistors: From High-Performance to Thin-Film Applications. *Science* **2015**, *349*, No. aab2750.

(22) Chhowalla, M.; Shin, H. S.; Eda, G.; Li, L.-J.; Loh, K. P.; Zhang, H. The Chemistry of Two-Dimensional Layered Transition Metal Dichalcogenide Nanosheets. *Nat. Chem.* **2013**, *5*, 263−275.

(23) Jariwala, D.; Sangwan, V. K.; Lauhon, L. J.; Marks, T. J.; Hersam, M. C. Emerging Device Applications for Semiconducting Two-Dimensional Transition Metal Dichalcogenides. *ACS Nano* **2014**, *8*, 1102−1120.

(24) Lipatov, A.; Wilson, P. M.; Shekhirev, M.; Teeter, J. D.; Netusil, R.; Sinitskii, A. Few-Layered Titanium Trisulfide (TiS_3) Field-Effect Transistors. *Nanoscale* **2015**, *7*, 12291−12296.

(25) Wang, Q. H.; Kalantar-Zadeh, K.; Kis, A.; Coleman, J. N.; Strano, M. S. Electronics and Optoelectronics of Two-Dimensional Transition Metal Dichalcogenides. *Nat. Nanotechnol.* **2012**, *7*, 699−712.

(26) Island, J. O.; Molina-Mendoza, A. J.; Barawi, M.; Biele, R.; Flores, E.; Clamagirand, J. M.; Ares, J. R.; Sánchez, C.; van der Zant, H. S. J.; D'Agosta, R.; Ferrer, I. J.; Castellanos-Gomez, A. Electronics and Optoelectronics of Quasi-1D Layered Transition Metal Trichalcogenides. *2D Mater.* **2017**, *4*, 022003.

(27) Randle, M. D.; Lipatov, A.; Mansaray, I.; Han, J. E.; Sinitskii, A.; Bird, J. P. Collective States and Charge Density Waves in the Group IV Transition Metal Trichalcogenides. *Appl. Phys. Lett.* **2021**, *118*, No. 210502.

(28) Stolyarov, M. A.; Liu, G.; Bloodgood, M. A.; Aytan, E.; Jiang, C.; Samnakay, R.; Salguero, T. T.; Nika, D. L.; Rumyantsev, S. L.; Shur, M. S.; Bozhilov, K. N.; Balandin, A. A. Breakdown Current Density in H-BN-Capped Quasi-1D $TaSe_3$ Metallic Nanowires: Prospects of Interconnect Applications. *Nanoscale* **2016**, *8*, 15774−15782.

(29) Abdulsalam, M.; Joubert, D. P. Structural and Electronic Properties of MX_3 (M = Ti, Zr and Hf; X = S, Se, Te) from First Principles Calculations. *Eur. Phys. J. B* **2015**, *88*, No. 177.

(30) Island, J. O.; Biele, R.; Barawi, M.; Clamagirand, J. M.; Ares, J. R.; Sánchez, C.; van der Zant, H. S. J.; Ferrer, I. J.; D'Agosta, R.; Castellanos-Gomez, A. Titanium Trisulfide (TiS_3): A 2D Semiconductor with Quasi-1D Optical and Electronic Properties. *Sci. Rep.* **2016**, *6*, No. 22214.

(31) Lipatov, A.; Loes, M. J.; Lu, H.; Dai, J.; Patoka, P.; Vorobeva, N. S.; Muratov, D. S.; Ulrich, G.; Kästner, B.; Hoehl, A.; Ulm, G.; Zeng, X. C.; Rühl, E.; Gruverman, A.; Dowben, P. A.; Sinitskii, A. Quasi-1D TiS_3 Nanoribbons: Mechanical Exfoliation and Thickness-Dependent Raman Spectroscopy. *ACS Nano* **2018**, *12*, 12713−12720.

(32) Muratov, D. S.; Vanyushin, V. O.; Vorobeva, N. S.; Jukova, P.; Lipatov, A.; Kolesnikov, E. A.; Karpenkov, D.; Kuznetsov, D. V.; Sinitskii, A. Synthesis and Exfoliation of Quasi-1D $(Zr,Ti)S_3$ Solid Solutions for Device Measurements. *J. Alloys Compd.* **2020**, *815*, No. 152316.

(33) Gilbert, S. J.; Yi, H.; Chen, J.-S.; Yost, A. J.; Dhingra, A.; Abourahma, J.; Lipatov, A.; Avila, J.; Komesu, T.; Sinitskii, A.; Asensio, M. C.; Dowben, P. A. Effect of Band Symmetry on Photocurrent Production in Quasi-One-Dimensional Transition-Metal Trichalcogenides. *ACS Appl. Mater. Interfaces* **2020**, *12*, 40525−40531.

(34) Pant, A.; Torun, E.; Chen, B.; Bhat, S.; Fan, X.; Wu, K.; Wright, D. P.; Peeters, F. M.; Soignard, E.; Sahin, H.; Tongay, S. Strong Dichroic Emission in the Pseudo One Dimensional Material ZrS_3. *Nanoscale* **2016**, *8*, 16259−16265.

(35) Muratov, D. S.; Ishteev, A. R.; Lypenko, D. A.; Vanyushin, V. O.; Gostishev, P.; Perova, S.; Saranin, D. S.; Rossi, D.; Auf der Maur, M.; Volonakis, G.; Giustino, F.; Persson, P. O. Å.; Kuznetsov, D. V.; Sinitskii, A.; Di Carlo, A. Slot-Die-Printed Two-Dimensional ZrS_3 Charge Transport Layer for Perovskite Light-Emitting Diodes. *ACS Appl. Mater. Interfaces* **2019**, *11*, 48021−48028.

(36) Zybtsev, S. G.; Pokrovskii, V.; Nasretdinova, V.; Zaitsev-Zotov, S.; Pavlovskiy, V.; Odobesco, A.; Pai, W.; Chu, M.; Lin, Y. G.; Zupanivč, E.; van Midden, H. J. P.; Šturm, S.; Tchernychova, E.; Prodan, A.; Bennett, J.; Mukhamedshin, I.; Chernysheva, O.; Menushenkov, A.; Loginov, V.; Loginov, B.; Titov, A. N.; Abdel-Hafiez, M. NbS_3: A Unique Quasi-One-Dimensional Conductor with Three Charge Density Wave Transitions. *Phys. Rev. B* **2017**, *95*, No. 035110.

(37) Geremew, A.; Bloodgood, M. A.; Aytan, E.; Woo, B. W. K.; Corber, S. R.; Liu, G.; Bozhilov, K.; Salguero, T. T.; Rumyantsev, S.; Rao, M. P.; Balandin, A. A. Current Carrying Capacity of Quasi-1D $ZrTe_3$ Van Der Waals Nanoribbons. *IEEE Electron Device Lett.* **2018**, *39*, 735−738.

(38) Island, J. O.; Buscema, M.; Barawi, M.; Clamagirand, J. M.; Ares, J. R.; Sánchez, C.; Ferrer, I. J.; Steele, G. A.; van der Zant, H. S. J.; Castellanos-Gomez, A. Ultrahigh Photoresponse of Few-Layer TiS_3 Nanoribbon Transistors. *Adv. Opt. Mater.* **2014**, *2*, 641−645.

(39) Bigg, D. M.; Stutz, D. E. Plastic Composites for Electromagnetic Interference Shielding Applications. *Polym. Compos.* **1983**, *4*, 40−46.

(40) Pan, Y.; Weng, G. J.; Meguid, S. A.; Bao, W. S.; Zhu, Z.-H.; Hamouda, A. M. S. Percolation Threshold and Electrical Conductivity of a Two-Phase Composite Containing Randomly Oriented Ellipsoidal Inclusions. *J. Appl. Phys.* **2011**, *110*, No. 123715.

(41) Molina-Mendoza, A. J.; Island, J. O.; Paz, W. S.; Clamagirand, J. M.; Ares, J. R.; Flores, E.; Leardini, F.; Sánchez, C.; Agraït, N.; Rubio-Bollinger, G.; van der Zant, H. S. J.; Ferrer, I. J.; Palacios, J. J.;

Castellanos-Gomez, A. High Current Density Electrical Breakdown of TiS_3 Nanoribbon-Based Field-Effect Transistors. *Adv. Funct. Mater.* **2017**, *27*, No. 1605647.

(42) Murphy, D. W.; Trumbore, F. A. The Chemistry of TiS_3 and $NbSe_3$ Cathodes. *J. Electrochem. Soc.* **1976**, *123*, 960−964.

(43) Kikkawa, S.; Koizumi, M.; Yamanaka, S.; Onuki, Y.; Tanuma, S. Electrical Conductivity of TiS_3. *Phys. Status Solidi A* **1980**, *61*, K55−K57.

(44) Hsieh, P.-L.; Jackson, C. M.; Grüner, G. Disorder Effects in the Linear Chain Compound TiS_3. *Solid State Commun.* **1983**, *46*, 505−507.

(45) Gorochov, O.; Katty, A.; Le Nagard, N.; Levy-Clement, C.; Schleich, D. M. Photoelectrochemical Study of TiS_3 in Aqueous Solution. *Mater. Res. Bull.* **1983**, *18*, 111−118.

(46) Finkman, E.; Fisher, B. Electrical Transport Measurements in TiS_3. *Solid State Commun.* **1984**, *50*, 25−28.

(47) Gorlova, I. G.; Pokrovskii, V. Y.; Zybtsev, S. G.; Titov, A. N.; Timofeev, V. N. Features of the Conductivity of the Quasi-One-Dimensional Compound TiS_3. *J. Exp. Theor. Phys.* **2010**, *111*, 298−303.

(48) Gorlova, I. G.; Zybtsev, S. G.; Pokrovskii, V. Y.; Bolotina, N. B.; Verin, I. A.; Titov, A. N. Nonlinear Conductivity of Quasi-One-Dimensional Layered Compound TiS_3. *Phys. B: Condens. Matter* **2012**, *407*, 1707−1710.

(49) Ferrer, I. J.; Maciá, M. D.; Carcelén, V.; Ares, J. R.; Sánchez, C. On the Photoelectrochemical Properties of TiS_3 Films. *Energy Procedia* **2012**, *22*, 48−52.

(50) Ferrer, I. J.; Ares, J. R.; Clamagirand, J. M.; Barawi, M.; Sánchez, C. Optical Properties of Titanium Trisulphide (TiS_3) Thin Films. *Thin Solid Films* **2013**, *535*, 398−401.

(51) Yi, H.; Komesu, T.; Gilbert, S.; Hao, G.; Yost, A.; Lipatov, A.; Sinitskii, A.; Ávila, J.; Chen, C.; Asensio, M.; Dowben, P. The Band Structure of the Quasi-One-Dimensional Layered Semiconductor $TiS_3(001)$. *Appl. Phys. Lett.* **2018**, *112*, 052102.

(52) Randle, M.; Lipatov, A.; Kumar, A.; Kwan, C.-P.; Nathawat, J.; Barut, B.; Yin, S.; He, K.; Arabchigavkani, N.; Dixit, R.; Komesu, T.; Avila, J.; Asensio, M. C.; Dowben, P. A.; Sinitskii, A.; Singisetti, U.; Bird, J. P. Gate-Controlled Metal−Insulator Transition in TiS_3 Nanowire Field-Effect Transistors. *ACS Nano* **2019**, *13*, 803−811.

(53) Cui, Q.; Lipatov, A.; Wilt, J. S.; Bellus, M. Z.; Zeng, X. C.; Wu, J.; Sinitskii, A.; Zhao, H. Time-Resolved Measurements of Photocarrier Dynamics in TiS_3 Nanoribbons. *ACS Appl. Mater. Interfaces* **2016**, *8*, 18334−18338.

(54) Dai, J.; Zeng, X. C. Titanium Trisulfide Monolayer: Theoretical Prediction of a New Direct-Gap Semiconductor with High and Anisotropic Carrier Mobility. *Angew. Chem., Int. Ed.* **2015**, *54*, 7572−7576.

(55) Dhingra, A.; Lipatov, A.; Loes, M. J.; Sinitskii, A.; Dowben, P. A. Nonuniform Debye Temperatures in Quasi-One-Dimensional Transition-Metal Trichalcogenides. *ACS Mater. Lett.* **2021**, *3*, 414−419.

(56) Ghatak, S.; Pal, A. N.; Ghosh, A. Nature of Electronic States in Atomically Thin MoS_2 Field-Effect Transistors. *ACS Nano* **2011**, *5*, 7707−7712.

(57) Wang, H.; Yu, L.; Lee, Y.-H.; Shi, Y.; Hsu, A.; Chin, M. L.; Li, L.-J.; Dubey, M.; Kong, J.; Palacios, T. Integrated Circuits Based on Bilayer MoS_2 Transistors. *Nano Lett.* **2012**, *12*, 4674−4680.

(58) Gorlova, I. G.; Pokrovskii, V. Y. Collective Conduction Mechanism in a Quasi-One-Dimensional TiS_3 Compound. *JETP Lett.* **2009**, *90*, 295−298.

(59) Frisenda, R.; Giovanelli, E.; Mishra, P.; Gant, P.; Flores, E.; Sánchez, C.; Ares, J. R.; de Lara, D.; Ferrer, I. J.; Pérez, E. M.; Castellanos-Gomez, A. Dielectrophoretic Assembly of Liquid-Phase-Exfoliated TiS_3 Nanoribbons for Photodetecting Applications. *Chem. Commun.* **2017**, *53*, 6164−6167.

(60) Nečas, D.; Klapetek, P. Gwyddion: An Open-Source Software for SPM Data Analysis. *Open Phys.* **2012**, *10*, 99.

(61) Wu, K.; Torun, E.; Sahin, H.; Chen, B.; Fan, X.; Pant, A.; Parsons Wright, D.; Aoki, T.; Peeters, F. M.; Soignard, E.; Tongay, S. Unusual Lattice Vibration Characteristics in Whiskers of the Pseudo-One-Dimensional Titanium Trisulfide TiS_3. *Nat. Commun.* **2016**, *7*, No. 12952.

(62) Galliardt, D. W.; Nieveen, W. R.; Kirby, R. D. Lattice Properties of the Linear Chain Compound TiS_3. *Solid State Commun.* **1980**, *34*, 37−39.

(63) Gard, P.; Cruege, F.; Sourisseau, C.; Gorochov, O. Single-Crystal Micro-Raman Studies of ZrS_3, TiS_3 and Several $Zr_{1-x}Ti_xS_3$ Compounds ($0<x\leqslant0.33$). *J. Raman Spectrosc.* **1986**, *17*, 283−288.

(64) Soltman, D.; Subramanian, V. Inkjet-Printed Line Morphologies and Temperature Control of the Coffee Ring Effect. *Langmuir* **2008**, *24*, 2224−2231.

(65) Derby, B. Inkjet Printing of Functional and Structural Materials: Fluid Property Requirements, Feature Stability, and Resolution. *Annu. Rev. Mater. Res.* **2010**, *40*, 395−414.

(66) Fromm, J. E. Numerical Calculation of the Fluid Dynamics of Drop-on-Demand Jets. *IBM J. Res. Dev.* **1984**, *28*, 322−333.

(67) Torrisi, F.; Hasan, T.; Wu, W.; Sun, Z.; Lombardo, A.; Kulmala, T. S.; Hsieh, G.-W.; Jung, S.; Bonaccorso, F.; Paul, P. J.; Chu, D.; Ferrari, A. C. Inkjet-Printed Graphene Electronics. *ACS Nano* **2012**, *6*, 2992−3006.

(68) Jang, D.; Kim, D.; Moon, J. Influence of Fluid Physical Properties on Ink-Jet Printability. *Langmuir* **2009**, *25*, 2629−2635.

(69) Hu, G.; Kang, J.; Ng, L. W. T.; Zhu, X.; Howe, R. C. T.; Jones, C. G.; Hersam, M. C.; Hasan, T. Functional Inks and Printing of Two-Dimensional Materials. *Chem. Soc. Rev.* **2018**, *47*, 3265−3300.

(70) Bonaccorso, F.; Bartolotta, A.; Coleman, J. N.; Backes, C. 2D-Crystal-Based Functional Inks. *Adv. Mater.* **2016**, *28*, 6136−6166.

(71) Shin, P.; Sung, J.; Lee, M. H. Control of Droplet Formation for Low Viscosity Fluid by Double Waveforms Applied to a Piezoelectric Inkjet Nozzle. *Microelectron. Reliab.* **2011**, *51*, 797−804.

(72) Dong, H.; Carr, W. W.; Morris, J. F. An Experimental Study of Drop-on-Demand Drop Formation. *Phys. Fluids* **2006**, *18*, 072102.

(73) de Gans, B.-J.; Kazancioglu, E.; Meyer, W.; Schubert, U. S. Ink-Jet Printing Polymers and Polymer Libraries Using Micropipettes. *Macromol. Rapid Commun.* **2004**, *25*, 292−296.

(74) Hu, G.; Albrow-Owen, T.; Jin, X.; Ali, A.; Hu, Y.; Howe, R. C. T.; Shehzad, K.; Yang, Z.; Zhu, X.; Woodward, R. I.; Wu, T.-C.; Jussila, H.; Wu, J.-B.; Peng, P.; Tan, P.-H.; Sun, Z.; Kelleher, E. J. R.; Zhang, M.; Xu, Y.; Hasan, T. Black Phosphorus Ink Formulation for Inkjet Printing of Optoelectronics and Photonics. *Nat. Commun.* **2017**, *8*, No. 278.

(75) Gilbert, S. J.; Lipatov, A.; Yost, A. J.; Loes, M. J.; Sinitskii, A.; Dowben, P. A. The Electronic Properties of Au and Pt Metal Contacts on Quasi-One-Dimensional Layered $TiS_3(001)$. *Appl. Phys. Lett.* **2019**, *114*, 101604.

(76) Baranovskii, S.; Rubel, O. Charge Transport in Disordered Materials. In *Springer Handbook of Electronic and Photonic Materials*; Kasap, S.; Capper, P., Eds.; Springer International Publishing: Cham, 2017; pp 193−218.

(77) Zubair Ansari, M.; Khare, N. Thermally Activated Band Conduction and Variable Range Hopping Conduction in Cu_2ZnSnS_4 Thin Films. *J. Appl. Phys.* **2015**, *117*, 025706.

(78) Chiu, F.-C. A Review on Conduction Mechanisms in Dielectric Films. *Adv. Mater. Sci. Eng.* **2014**, *2014*, No. 578168.

(79) Mott, N. F. Conduction in Glasses Containing Transition Metal Ions. *J. Non-Cryst. Solids* **1968**, *1*, 1−17.

(80) Efros, A. L.; Shklovskii, B. I. Coulomb Gap and Low Temperature Conductivity of Disordered Systems. *J. Phys. C: Solid State Phys.* **1975**, *8*, L49−L51.

(81) Kumar, R.; Khare, N. Temperature Dependence of Conduction Mechanism of ZnO and Co-Doped ZnO Thin Films. *Thin Solid Films* **2008**, *516*, 1302−1307.

(82) Prudenziati, M.; Hormadaly, J. *Printed Films: Materials Science and Applications in Sensors, Electronics and Photonics*; Elsevier Science & Technology: Cambridge, United Kingdom, 2012.

(83) Wang, F.; Gosling, J. H.; Trindade, G. F.; Rance, G. A.; Makarovsky, O.; Cottam, N. D.; Kudrynskyi, Z.; Balanov, A. G.; Greenaway, M. T.; Wildman, R. D.; Hague, R.; Tuck, C.; Fromhold,

T. M.; Turyanska, L. Inter-Flake Quantum Transport of Electrons and Holes in Inkjet-Printed Graphene Devices. *Adv. Funct. Mater.* **2021**, *31*, No. 2007478.

(84) Geremew, A.; Qian, C.; Abelson, A.; Rumyantsev, S.; Kargar, F.; Law, M.; Balandin, A. A. Low-Frequency Electronic Noise in Superlattice and Random-Packed Thin Films of Colloidal Quantum Dots. *Nanoscale* **2019**, *11*, 20171−20178.

(85) Guyot-Sionnest, P. Electrical Transport in Colloidal Quantum Dot Films. *J. Phys. Chem. Lett.* **2012**, *3*, 1169−1175.

(86) Mohammadzadeh, A.; Rehman, A.; Kargar, F.; Rumyantsev, S.; Smulko, J. M.; Knap, W.; Lake, R. K.; Balandin, A. A. Room Temperature Depinning of the Charge-Density Waves in Quasi-Two-Dimensional 1T-TaS_2 Devices. *Appl. Phys. Lett.* **2021**, *118*, No. 223101.

(87) Ghosh, S.; Kargar, F.; Mohammadzadeh, A.; Rumyantsev, S.; Balandin, A. A. Low-Frequency Electronic Noise Spectroscopy of Quasi-2D van Der Waals Antiferromagnetic Semiconductor $FePS_3$ — Signatures of Phase Transitions. *Adv. Electron. Mater.* **2021**, 2100408.

(88) Geremew, A. K.; Rumyantsev, S.; Debnath, B.; Lake, R. K.; Balandin, A. A. High-Frequency Current Oscillations in Charge-Density-Wave 1T-TaS_2 Devices: Revisiting the "Narrow Band Noise" Concept. *Appl. Phys. Lett.* **2020**, *116*, No. 163101.

(89) Salgado, R.; Mohammadzadeh, A.; Kargar, F.; Geremew, A.; Huang, C.-Y.; Bloodgood, M. A.; Rumyantsev, S.; Salguero, T. T.; Balandin, A. A. Low-Frequency Noise Spectroscopy of Charge-Density-Wave Phase Transitions in Vertical Quasi-2D 1T-TaS_2 Devices. *Appl. Phys. Express* **2019**, *12*, No. 037001.

(90) Liu, G.; Rumyantsev, S.; Bloodgood, M. A.; Salguero, T. T.; Balandin, A. A. Low-Frequency Current Fluctuations and Sliding of the Charge Density Waves in Two-Dimensional Materials. *Nano Lett.* **2018**, *18*, 3630−3636.

(91) Balandin, A. A. *Noise and Fluctuations Control in Electronic Devices*; American Scientific Publishers, 2002.